Supplementary Information for

Roles of soluble species in the alkaline oxygen evolution reaction on a nickel anode

Jia-Ming Ye, Ding-Hong He, Fang Li, Yu-Lin Li and Jian-Bo He*

Anhui Province Key Laboratory of Advanced Catalytic Materials and Reaction Engineering, School of Chemistry and Chemical Engineering, Hefei University of Technology, Hefei 230009, China. E-mail: jbhe@hfut.edu.cn

S1 Experimental Detail

S1.1 Materials and Apparatus

$NiCl_2 \cdot 6H_2O$, boric acid, NaOH (Fe ≤ 0.001 w%), Na-phytate (>98%) and H_2SO_4 were of analytical grade from Sinopharm Group and used as received. High pure nickel sheet (>99.99%), spectrograde graphite powder (325 mesh) and spectrograde paraffin wax (solidification point 62–65°C) were used for fabricating the working electrodes. Doubly-distilled water was used for making up all solutions and to rinse electrodes. High pure N_2 was used to deaerate the solution.

All electrochemical measurements were carried out on a CHI 760D electrochemical workstation (CH Instruments, USA). UV–vis absorption spectra and chronoabsorptometric data were measured using a model UV-2500 spectrophotometer with UV probe data software (Shimadzu, Japan). X-ray photoelectron spectra (XPS) were measured on an EscaLab 250Xi spectrometer fitted with a monochromatic Al Kα X-ray source ($h\nu$ = 1486.6 eV). The spectra were accumulated at a pressure of less than 10^{-8} mbar. The C 1s line of adventitious carbon at 285 eV was used as internal standard to calibrate the binding energies. The morphologies of the electrode surfaces were characterized on a field emission scanning electron microscope (Zeiss Merlin and SUPRA 40 Zeiss, operated at an acceleration voltage of 5.00 kV).

S1.2 Electrodes and Cells

The three-electrode systems for electrochemical and spectroelectrochemical measurements were composed of a nickel working electrode, an $Ag/AgCl/KCl_{sat}$ reference electrode and a platinum–coil auxiliary electrode. All potentials reported in this work were converted to the reversible hydrogen electrode (RHE) in the working electrolyte according to the relationship between the two scales

($E_{RHE} = E_{Ag/AgCl} + 0.0591pH + 0.197$ V). A nickel sheet electrode with a geometric area of 0.5 cm^2 was used for conventional electrochemical tests and surface characterization. This common nickel electrode is unsuitable as a working electrode for the thin-layer spectroelectrochemistry, because it may produce high concentration of soluble ions into the thin-layer, beyond the measurable limit of spectrophotometer. For this consideration, a small amount of nickel was electrodeposited on an inert substrate, i.e. a solid carbon paste electrode (sCPE) with a size of 9.8 × 8.0 cm^2, which was made from graphite powder and paraffin wax.[1] The such-prepared nickel electrode is denoted as Ni/sCPE.

A 50-ml volume single-compartment cell was used for the conventional electrochemical measurements. The thin-layer spectroelectrochemical cell was constructed as reported in the literature.[2] The cell body is a standard square quartz cell with 10 mm optical path length, in which the square Ni/sCPE and a self-made miniature $Ag/AgCl/KCl_{sat}$ were assembled. The thin-layer electrolysis chamber with a volume of 10 μL (10 × 10 × 0.1 mm^3) is located between the Ni/sCPE plate and a PTFE plate with nine ϕ0.1 mm holes as current channels. The incident light passes between the two plates and through the thin-layer electrolyte. The incident direction parallel to the electrode surface allows an opaque electrode to be used. The time constant of the cell was less than 1 ms in 0.5 M KCl, which was characterized by chronoamperometric experiments.

S1.3 Procedures

Before each use, the electrode was polished with emery papers, using 2000 grit for the nickel sheet and 800 grit for both sCPE and Ni/sCPE, followed by rinsing thoroughly with distilled water. Then the electrochemical cleaning was performed by 100 s potentiostatic reduction at –0.5 V (vs. RHE) in 0.1 M NaOH for the nickel sheet electrodes, or by 30 cycles potential cycling in 1.0 M KCl between 0.0 and 2.0 V (vs. RHE) at 0.5 V s^{-1} for the bare sCPE. The Ni/sCPE was prepared by depositing metal nickel from a solution of 0.01 M $NiCl_2$ and 0.5 M H_3BO_3, at a constant current density of 1.0 mA cm^{-2} for 60 s; the electric charge consumed corresponds to a theoretical Ni thickness of 20 nm.

The anodic processes of nickel including the oxygen evolution were investigated in 0.1 and 1.0 M NaOH, which were bubbled with N_2 for about 15 min to remove dissolved oxygen. For the Fe effect study, Fe(III) ions were introduced up to a concentration of 0.056-2.8 ppm Fe(III) by injecting several microliters of 5 or 50 mM $Fe_2(SO_4)_3$ into 20 ml of NaOH electrolytes. For rigorously Fe-free measurements, 700 mg of newly-prepared solid $Ni(OH)_2$ was added to 30 ml of NaOH electrolytes to adsorb Fe impurities, according to the purification method developed by Trotochaud et al.[3] The mixtures were mechanically agitated for at least 10 min, followed by at least 3 h of resting. After centrifuged, 20 ml of purified NaOH supernatant was decanted into a H_2SO_4-cleaned polypropylene cell for CV measurement. For introducing Ni(II) ions without Fe removal, only 3 or 5 mg of newly-prepared $Ni(OH)_2$ was completely dissolved into 50 ml of 0.1 or 1.0 M NaOH under ultrasound for 1 h. The electrolyte treatments were performed in closed container to

avoid solvent evaporation.

Cyclic voltammetry (CV), single linear sweep voltammetry, electrochemical impedance spectroscopy (EIS) and chronopotentiometry were performed under unstirring and stirring conditions. For the stirring, a magnetic stirrer was operated at a constant rotating rate of 250 rpm. For the spectroelectrochemical experiments, a 1.0 mL portion of NaOH solution was injected into the thin-layer chamber of the cell and then partly infiltrated into the two side chambers, ensuring no gas bubble in the thin layer. The *in situ* UV–vis absorption spectra were recorded during the potentiostatic oxidation. Thin-layer cyclic voltabsorptometry (CVA) coupled with CV was performed at a certain wavelength to follow the concentration changes of the solution species in the thin layer. All experiments were conducted at room temperature (22 °C).

S2 Activation at a constant potential

The Ni anode activation can occur at a constant OER potential. Fig. S1a shows the chronoamperometric transients for the OER in 0.1 M NaOH at 1.65 V (vs. RHE). In the unstirred solution, the current density increased with time up to about 3 h, mainly at the initial stage of reaction (48 min, curve 1). In the stirred solution, however, the current rise lasted only for 16 min, mainly in the initial 6 min (curve 2). Therefore, the activation of the Ni anode can be greatly accelerated by stirring. We deduce that the activation should be related to the diffusion of soluble species in the diffusion layer, although the activation has been generally attributed to a transition from the α-$Ni(OH)_2$/γ-NiOOH solid-state redox couple to the β-$Ni(OH)_2$/β-NiOOH couple.[4-6]

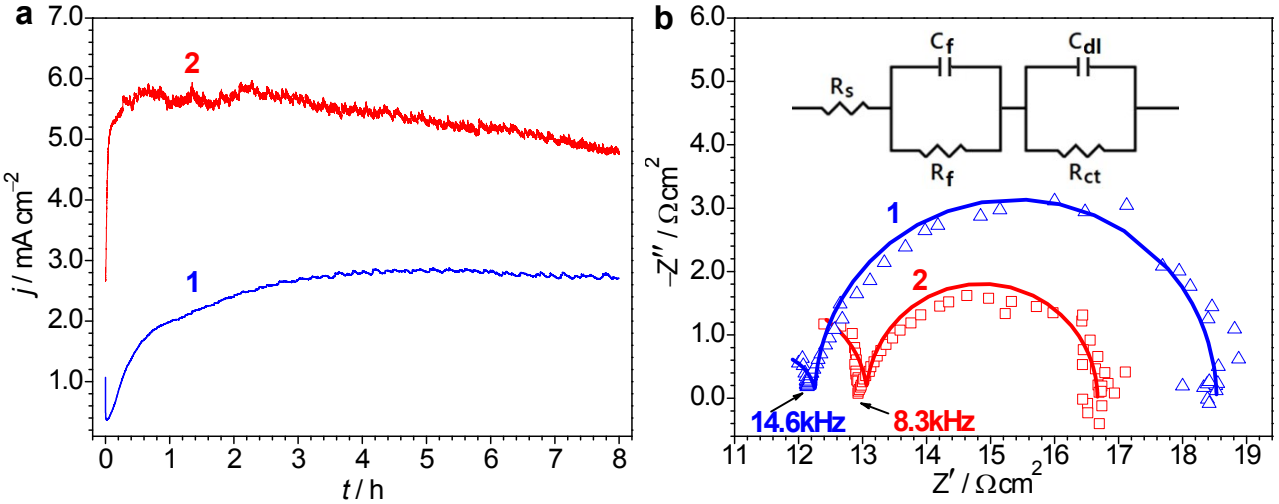

Fig. S1 (a) Chronoamperometric transients of Ni anode at 1.65 V (vs. RHE) in 0.1 M NaOH without (1) and with (2) stirring; (b) Experimental (symbols) and simulated (solid lines) Nyquist plots recorded after oxidation at 1.65 V for 0 (1) and 30 min (2), bias potential: 1.65 V vs. RHE, frequency range: 100 kHz – 0.1 Hz, amplitude: 5 mV; inset: the equivalent circuit for data fitting.

The potentiostatic activation of the Ni anode was further characterized by EIS, as shown in Fig.

S1b. The Nyquist plots show the characteristics of two capacitance loops. The high-frequency one is very incomplete and small in diameter. This loop is related to the dielectric performance of the Ni oxide layer, whereas the low-frequency one to the OER occurring on the surface film. The EIS data were fitted by using the equivalent electrical circuit in the inset of Fig. S1b. In the circuit, R_s is the solution resistance and the high-frequency circuit C_f–R_f corresponds to the capacitance and resistance of the oxide layer;[7] the low frequency circuit C_{dl}–R_{ct} represents the double-layer capacitance and charge transfer resistance of the OE R. The parameters obtained for the equivalent circuit elements are listed in Table S1. The activation of 30 min at 1.65 V led to a decrease of R_{ct} from 6.28 to 3.61 Ω cm^2 and an increase of C_{dl} from 246 to 281 μF cm^{-2}. The magnitude of C_{dl} is proportional to real surface area of the Ni oxide film.

Table S1 Model parameters simulated from the experimental EIS data in Fig. S1b. The values in parentheses are the percentage errors in the fitting parameters.

Activation time / min	R_s /Ω cm^2	C_f /μF cm^{-2}	R_f /Ω cm^2	C_{dl} /μF cm^{-2}	R_{ct} /Ω cm^2
0	10.9 (4.8)	0.798 (77)	1.40 (37)	246 (2.6)	6.28 (1.1)
30	10.0 (6.2)	0.325 (42)	3.04 (20)	281 (4.0)	3.61 (1.6)

S3 Ultrathin nature of Ni oxide film characterized by FE-SEM, XRD and XPS

The morphologies of nickel sheet electrodes were examined by FE-SEM before and after potentiostatic oxidation in 0.1 M NaOH at 1.65 V (vs. RHE) for 10 min, as shown in Fig. S2. No distinguishable deposit coating was observed at the oxidized surface. XRD pattern (Fig. S3) reveals two prominent peaks at 76.4° and 51.9° and a weak peak at 44.5° that match well face centered cubic nickel crystals (JCPDS 01-1260).[8] No other peaks (even a diffuse peak) were observed, confirming that the oxide film is too thin to be detected by XRD.

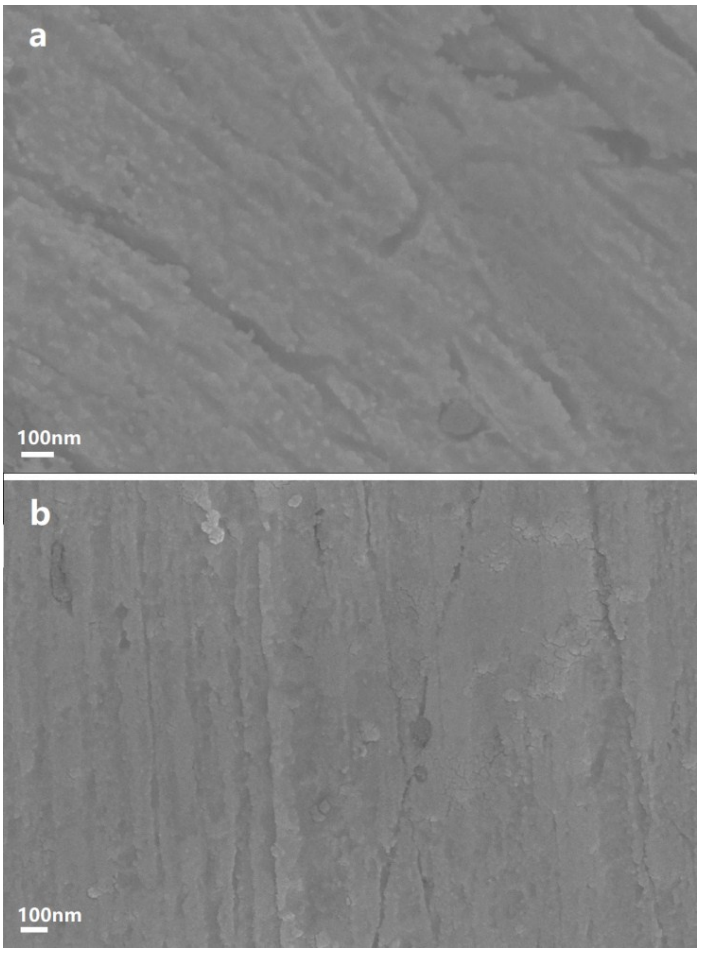

Fig. S2 FE-SEM images of the nickel sheet electrodes before (a) and after (b) potentiostatic oxidation in 0.1 M NaOH at 1.65 V (vs. RHE) for 10 min.

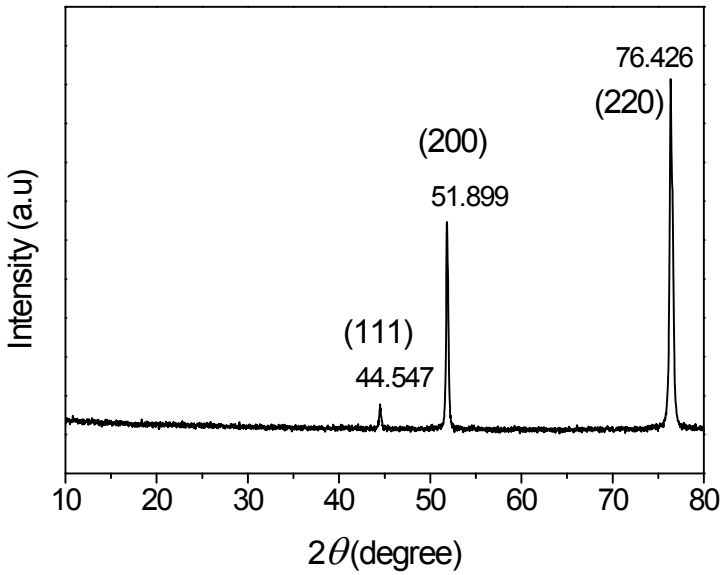

Fig. S3 XRD pattern of the nickel sheet electrode after potentiostatic oxidation in 0.1 M NaOH at 1.65 V (vs. RHE) for 60 min.

XPS spectra characterizing the surface state of nickel coating deposited at 1.65 V for 1 h in 0.1 M NaOH are presented in Fig. S4. The $Ni2p_{3/2}$ peak around 856 eV along with its satellite peak around 816 eV can be diconvoluted into four peaks (Fig. S4a), i.e., peak I (852.9 eV, Ni),[9,10] peak II (854.3 eV, NiO),[11] peak III (855.9 eV, $Ni(OH)_2$),[12] and peak IV (857 eV, Ni_2O_3).[13,14] Correspondingly, the satellite features present on the spectra at binding energies (E_b) of 858.5, 861.1, 861.7 and 863.7 eV are attributed to $Ni2p_{3/2}$ for Ni^0, NiO, $Ni(OH)_2$ and Ni_2O_3,[10-13] respectively. The presence of the small peak I assigned to Ni^0 indicates that the oxide coating on the substrate Ni was very thin, not exceeding the escape depth of XPS electrons.

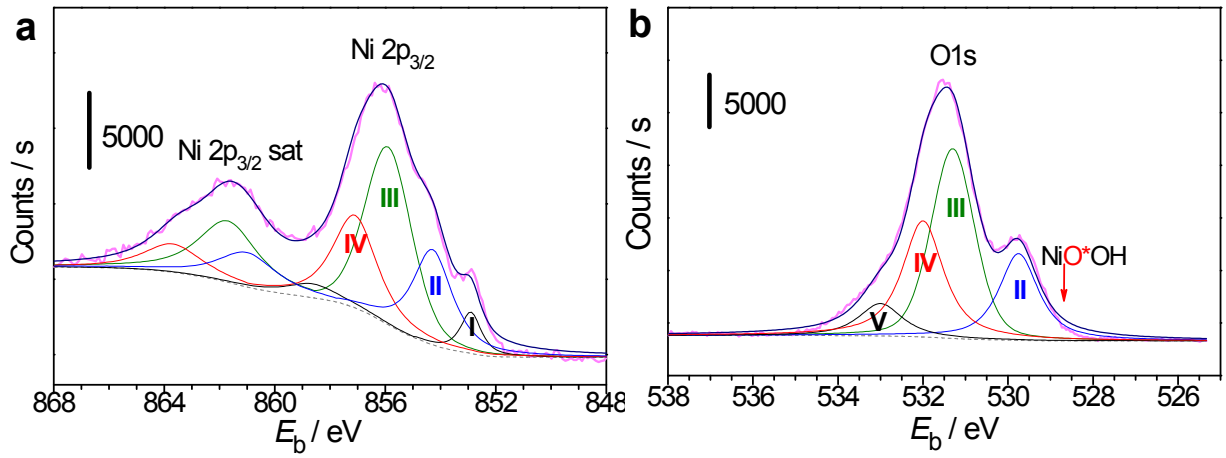

Fig. S4 XPS spectra of the Ni 2p3/2 (a) and O 1s (b) for the nickel electrodes after subjected to pre-oxidization at 1.65 V (vs. RHE) for 1 h in 0.1 M NaOH.

The O1s peak centered at 531.5 eV can also be deconvoluted into four peaks (Fig. S4b), i.e., peak II (529.7 eV, NiO),[15-17] peak III (531.3eV, $Ni(OH)_2$),[15-17] peak IV (532 eV, Ni_2O_3),[14] and peak V (533 eV, H_2O).[18] The small peak V at 533 eV may be due to adsorbed water or possibly adsorbed O_2. The O1s peak of NiO*OH (528.7 eV)[19] is not observed on the spectra (see the arrow in Fig. S4b), suggesting the absence of NiOOH in the *ex situ* prepared samples.

Both the $Ni2p_{3/2}$ and O1s peaks clearly show that the main component of the as-deposited nickel oxide coating is $Ni(OH)_2$. Park et al. demonstrated that, near the transpassivation region, the nickel metal at the metal oxide interface was not directly oxidized to NiOOH, but passing through $Ni(OH)_2$ as the intermediate.[20] A small NiO layer was also present, which has been detected between the $Ni(OH)_2$ and metallic nickel substrate by Alsabet et al.[21] However, the trivalent species detected by XPS was Ni_2O_3, instead of NiOOH. It seems that NiOOH is dehydrated later to form Ni_2O_3 during the movement of the electrode to carry out XPS analysis under high vacuum conditions.[22]

S4 Presence of Fe on the surfaces of $Ni(OH)_2$/NiOOH

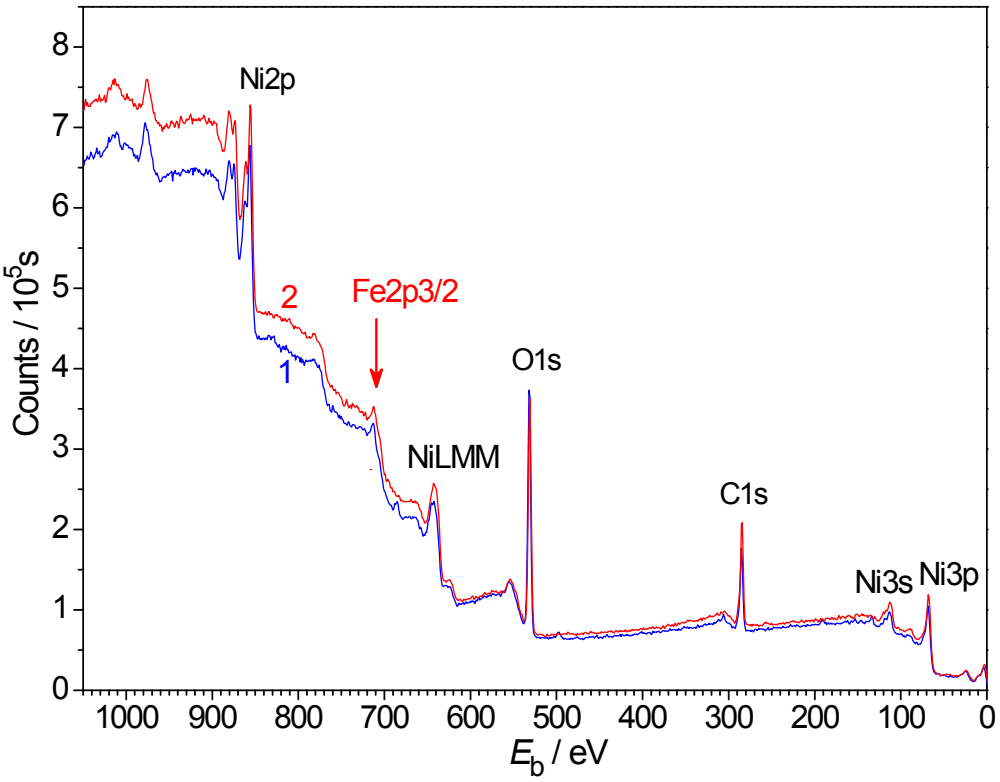

Fig. S5 XPS survey scan spectra for the nickel electrodes after subjected to oxidization at 1.65 V (vs. RHE) for 1 h in 0.1 M NaOH (1) and Ni(II)-saturated 0.1 M NaOH (2). The results show that the Ni(II) in electrolyte cannot inhibit the adsorption of Fe onto the Ni oxide surface.

S5 Effect of phytate on the OER activity

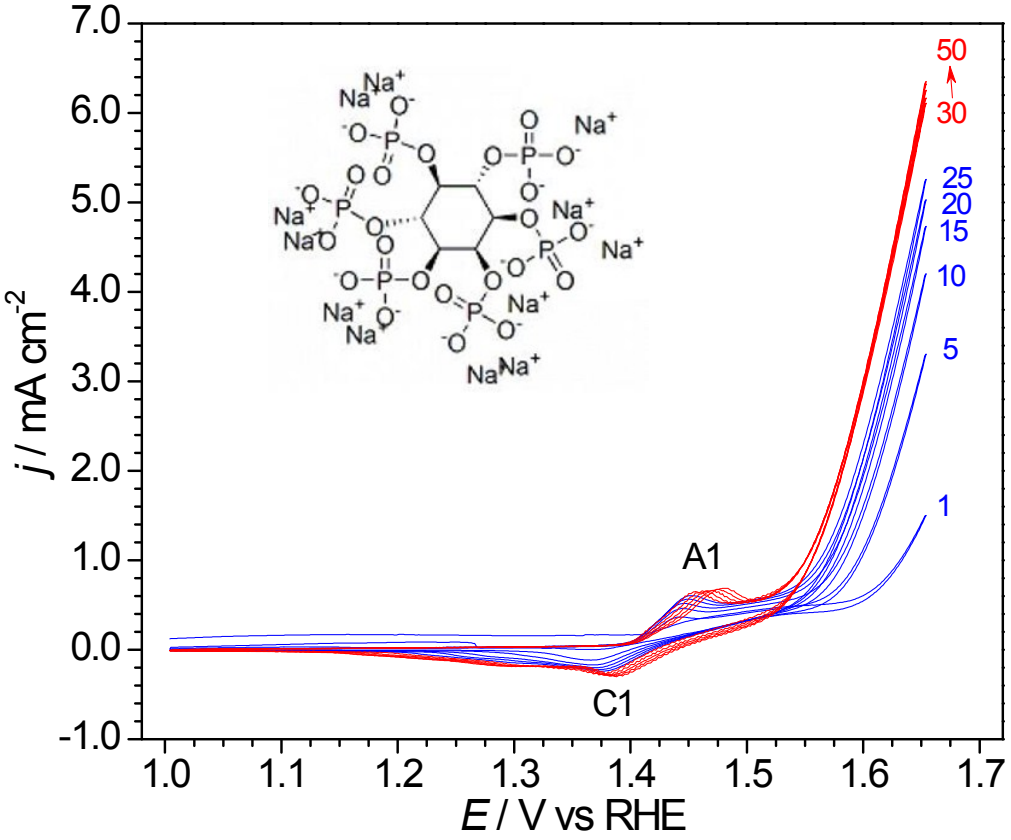

Fig. S6 Multi-cycle CVs at 10 mV s^{-1} for Ni electrode in 0.1 M NaOH + 10 mM $NaIP_6$. The first 25 (blue) and the second 25 (red) cycles were recorded under unstirring and stirring, respectively. The inset is the structural formula of $NaIP_6$. The OER current was significantly increased due to the addition of $NaIP_6$, in comparison with the results without IP6 (Fig. 1). Stirring is less effective than in the absence of IP_6, suggesting a faster removal of the soluble oxidation products [e.g., Ni(II)] due to the action of IP_6.

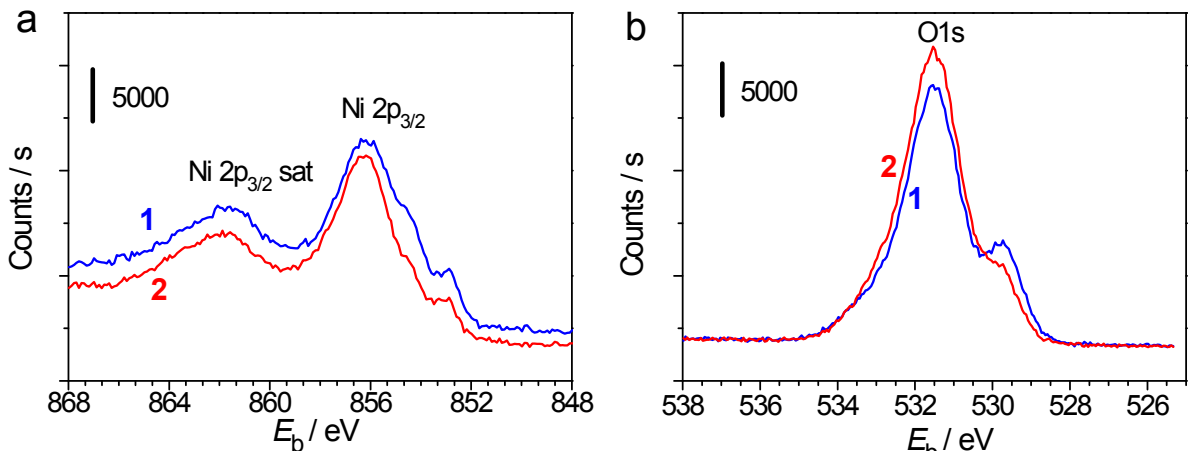

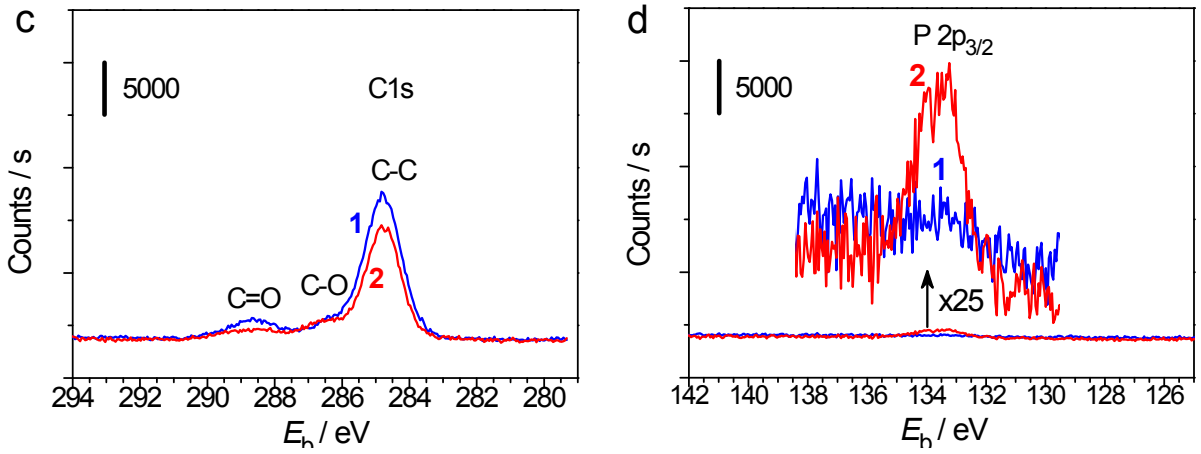

Fig. S7 XPS spectra of the Ni 2p3/2 (a), O 1s (b), C 1s (c), P 2p3/2 (d) for the nickel electrodes after oxidized at 1.65 V (vs. RHE) for 1 h in 0.1 M NaOH (1) and 0.1 M NaOH + 10 mM $NaIP_6$ (2). The results show that the Ni oxide film adsorbed only extremely trace amounts of IP_6 that did not change the film compositions.

S6 Catalytic mechanism

Jagannadham described the nature of the reactive species of the Ni(III) ions in a treatise on electron transfer reactions.[23] The Ni(III), as one electron abstractor, can oxidize iodide and thiocyanate anions, hydroxylamine, hydrazine, primary and secondary aliphatic alcohols, 1,2-diols, benzaldehydes, lactic acid, mandelic acid and ethanolamines, etc. The $Ni(OH)^{2+}$ ion was assumed to be the reactive form of Ni(III) generated from the dissolution of solid NiOOH in acidic media.[23] The trivalent Ni ion is reduced to the divalent state. In the present alkaline anodic system, a possible OER mechanism can be depicted as follows:

$$Ni(OH)_2\ (s) + OH^- \rightarrow NiOOH\ (s) + H_2O + e^- \quad (S1)$$

$$NiOOH\ (s) + H_2O \rightarrow NiOOH{\cdot}H_2O\ (s) \rightarrow Ni(OH)_3\ (aq) \quad (S2)$$

$$NiOOH{\cdot}H_2O\ (s)\ \text{or}\ Ni(OH)_3\ (aq) + S\text{-}(OH^-)_{ads} \rightarrow Ni(OH)_3^-\ (aq) + S\text{-}OH_{ads} \quad (S3)$$

$$S\text{-}OH_{ads} + OH^- \xrightarrow{OER} S\text{-}O_{ads} + H_2O + e^- \quad (S4)$$

$$2S\text{-}O_{ads} \rightarrow O_2 \quad (S5)$$

The symbol S represents the active sites adsorbing OH^- ions for the formation of oxygen. This mechanism does not deny the role of Fe in crystalline $Fe_xNi_{1-x}OOH$ phase in improving the catalytic activity of the active sites.

Either $NiOOH{\cdot}H_2O$ (s) (hydrous top layer) or $Ni(OH)_3$ (aq) is assumed to be the reactive form of Ni(III) in strong alkaline media. The reactive Ni(III) convert into Ni(II) ions, representatively $Ni(OH)_3^-$ (aq),[24] by capturing electrons from the adsorbed OH^- ions. The resulting OH radicals are anodically oxidized to generate adsorbed O atoms, once the potential is scanned into the OER

region. The O atoms then combine each other to produce oxygen molecules.[25,26] The aqueous Ni(II) product of reaction (S3) is electrochemically stable in the whole tested potential region, as reflected by the CVA results (Fig. 4b). The above mechanism based on aqueous Ni species offers the advantage of being able to explain the following observations:

The finding that the nickel (oxy)hydroxide film dissolves at an increasing rate with increasing cycle number (Fig. 4b) provides a new explanation for the OER performance enhanced by repetitive potential cycling across the main Ni(II/III) redox peaks at a slow scan rate.[5] $Ni(OH)_2$ and NiOOH dissolution can be favored by the oxidation process itself since this brings about an increase of surface polarity, producing significant tensile stresses compared to the pristine oxide.[27] As a consequence of that, the electromechanical tensions associated with the increase of charge density at the surface of the oxidized coating are relieved through the partial dissolution of the oxide film.[28]

The time required for the electrode activation can be greatly reduced by stirring the solution (Fig. S1a), because the stirring can accelerate the stripping of the Ni(II) species off the electrode surface and then promote the dissolution of the Ni (oxy)hydroxide film. As one of the anodic products, the Ni(II) accumulated in the diffusion layer exerts an inhibitory effect on the reaction (S3) and thus effectively inhibits the OER, as proved in Fig. 2, curves 8 and 9. In addition, the Ni(II) species may compete for the adsorption sites with the loosely adsorbed $Ni(OH)_3$.

At the starting potential of 1.75 V (vs. RHE) as in the inset of Fig. 1, an equilibrium between electrochemical formation [Eqn. (S1)] and chemical dissolution [Eqn. (S2)] was reached for NiOOH after 10 min of potentiostatic activation. As the potential was scanned negatively, the formation rate of NiOOH decreased, but its dissolution rate was potential-independent (inset of Fig. 3b). Thus the amount of NiOOH on the electrode surface gradually decreased during the backward scan, leading to the disappearance of its reduction peaks at the scan rate slow enough (inset of Fig. 1). In this case, Eqns. (S1) and (S2) can be merged into Eqn. (S2′), since the rate of reaction (S2) was larger than that of reaction (S1).

$$Ni(OH)_2\ (s) + OH^- \rightarrow Ni(OH)_3\ (aq) + e^- \qquad (S2')$$

The reaction (S2′) explains the OER current independent of the amount of solid NiOOH (the area of the cathodic peak in inset of Fig. 1).

Bell et al. proposed that β-NiOOH itself may not be the actual catalyst for OER, because β-NiOOH appears to convert to an unidentified form of Ni oxide at potentials above ~0.52 V (vs. Hg/HgO reference).[29] The Eqn. (S2) describes a conversion of solid NiOOH to a hydrous top layer and then to a solution state. The chemical identity of the very top layers of oxide films plays a more significant role in determining the OER kinetics.[26]

Tafel linearization of the polarization curves in the inset of Fig. 1 leads to a Tafel slope of about 51 mV dec^{-1}. Different Tafel slopes implicate different rate-determining steps. If the rate-determining step is the chemical reaction (S2) after the one-electron transfer reaction (S1), we can expect a Tafel slope close to 60 mV dec^{-1}.[25]

References

1 H. Gao, J.-B. He, Y. Wang and N. Deng, *J. Power Sources*, 2012, **205**, 164-172.

2 J.-B. He, Y. Wang, N. Deng and X.-Q. Lin, *Bioelectrochemistry*, 2007, **71**, 157-163.

3 L. Trotochaud, S. L. Young, J. K. Ranney and S. W. Boettcher, *J. Am. Chem. Soc.*, 2014, **136**, 6744-6753.

4 S. R. Mellsop, A. Gardiner, B. Johannessen and A. T. Marshall, *Electrochim. Acta*, 2015, **168**, 356-364.

5 I. J. Godwin and M. E. G. Lyons, *Electrochem. Commun.*, 2013, **32**, 39-42.

6 S. R. Mellsop, A. Gardiner and A. T. Marshall, *Electrochim. Acta*, 2015, **180**, 501-506.

7 X. Liao, F. Cao, L. Zheng, W. Liu, A. Chen, J. Zhang and C. Cao, *Corros. Sci.*, 2011, **53**, 3289-3298.

8 S. Chen, J. Duan, J. Ran, M. Jaroniec and S. Z. Qiao, *Energ. Environ. Sci.*, 2013, **6**, 3693-3699.

9 S. Tao, F. Yang, J. Schuch, W. Jaegermann and B. Kaiser, *ChemSusChem*, 2018, **11**, 948-958.

10 A. N. Mansour, *Surf. Sci. Spectra*, 1994, **3**, 221-230.

11 A. N. Mansour, *Surf. Sci. Spectra*, 1994, **3**, 231-238.

12 A. N. Mansour, *Surf. Sci. Spectra*, 1994, **3**, 239-246.

13 K. T. Ng and D. M. Hercules, *J. Phys. Chem.*, 1976, **80**, 2094-2102.

14 H. Liu, W. Zheng, X. Yan and B. Feng, *J. Alloy. Compd.*, 2008, **462**, 356-361.

15 J. Haber, J. Stoch and L. Ungier, *J. Electron Spectrosc. Relat. Phenom.*, 1976, **9**, 459-467.

16 J. F. Moulder, W. F. Stickle, P. E. Sobol and K. E. Bomben, *Handbook of X-ray photoelectron spectroscopy*, Physical Electronics, Eden Prairie, 1995.

17 S. V. Green, M. Watanabe, N. Oka, G. A. Niklasson, C. G. Granqvist and Y. Shigesato, *Thin Solid Films*, 2012, **520**, 3839-3842.

18 C. D. Wagner, D. A. Zatko and R. H. Raymond, *Anal. Chem.*, 1980, **52**, 1445-1451.

19 A. N. Mansour and C. A. Melendres, *Surf. Sci. Spectra*, 1994, **3**, 271-278.

20 Z. Chaojiong and P. Su-Moon, *J. Electrochem. Soc.*, 1987, **134**, 2966-2970.

21 M. Alsabet, M. Grden and G. Jerkiewicz, *Electrocatalysis*, 2014, **5**, 136-147.

22 A. Zaky, F. H. Assaf and F. E. Z. A. H. Ali, *Int. Sch. Res. Net.*, 2011, Article ID 356863, 1-6.

23 V. Jagannadham, *J. Am. Chem.*, 2012, **2**, 57-82.

24 B. Beverskog and I. Puigdomenech, *Corros. Sci.*, 1997, **39**, 969-980.

25 N.-T. Suen, S.-F. Hung, Q. Quan, N. Zhang, Y.-J. Xu and H. M. Chen, *Chem. Soc. Rev.*, 2017, **46**, 337-365.

26 P. W. T. Lu and S. Srinivasan, *J. Electrochem. Soc.*, 1978, **125**, 1416-1422.

27 D. Dini and F. Decker, *Electrochim. Acta*, 1998, **43**, 2919-2923.

28 A. G. Marrani, V. Novelli, S. Sheehan, D. P. Dowling and D. Dini, *ACS Appl. Mater. Inter.*, 2014, **6**, 143-152.

29 B. S. Yeo and A. T. Bell, *J. Phys. Chem. C*, 2012, **116**, 8394-8400.